Assessing muscle invasion in bladder cancer via virtual biopsy: a study on quantitative parameters and classical radiomics features from dual-energy CT imaging

Mengting Hu[1†], Wei Wei[1†], Jingyi Zhang[1], Shigeng Wang[1], Xiaoyu Tong[1], Yong Fan[1], Qiye Cheng[1], Yijun Liu[1], Jianying Li[2] and Lei Liu[3*]

Abstract

Objective To evaluate the prediction value of Dual-energy CT (DECT)-based quantitative parameters and radiomics model in preoperatively predicting muscle invasion in bladder cancer (BCa).

Materials and methods A retrospective study was performed on 126 patients with BCa who underwent DECT urography (DECTU) in our hospital. Patients were randomly divided into training and test cohorts with a ratio of 7:3. Quantitative parameters derived from DECTU were identified through univariate and multivariate logistic regression analysis to construct a DECT model. Radiomics features were extracted from the 40, 70, 100 keV and iodine-based material-decomposition (IMD) images in the venous phase to construct radiomics models from individual and combined images using a support vector machine classifier, and the optimal performing model was chosen as the final radiomics model. Subsequently, a fusion model combining the DECT parameters and the radiomics model was established. The diagnostic performances of all three models were evaluated through receiver operating characteristic (ROC) curves and the clinical usefulness was estimated using decision curve analysis (DCA).

Results The normalized iodine concentration (NIC) in DECT was an independent factor in diagnosing muscle invasion of BCa. The optimal multi-image radiomics model had predictive performance with an area-under-the-curve (AUC) of 0.867 in the test cohort, better than the AUC = 0.704 with NIC. The fusion model showed an increased level of performance, although the difference in AUC (0.893) was not statistically significant. Additionally, it demonstrated superior performance in DCA. For lesions smaller than 3 cm, the fusion model showed a high predictive capability, achieving an AUC value of 0.911. There was a slight improvement in model performance, although the difference was not statistically significant. This improvement was observed when comparing the AUC values of the DECT and radiomics models, which were 0.726 and 0.884, respectively.

†Mengting Hu and Wei Wei contributed equally to this work and share the first authorship.

*Correspondence:
Lei Liu
liuleidmu1989@163.com

Full list of author information is available at the end of the article

Conclusion The proposed fusion model combing NIC and the optimal multi-image radiomics model in DECT showed good diagnostic capability in predicting muscle invasiveness of BCa.

Keywords Urinary bladder neoplasms, Muscles, Dual-energy CT, Radiomics

Introduction

Bladder cancer (BCa) ranks as one of the most prevalent urologic malignancies and is the 10th most common cancer globally [1, 2]. The incidence of BCa is higher in men, where it stands as the 6th most common cancer and the 9th leading cause of cancer-related deaths [2]. In developed nations, around two-thirds of BCa cases manifest as non-muscle-invasive BCa (NMIBC), with the remaining cases presenting as muscle-invasive BCa (MIBC) [3]. The extent of muscle invasion serves as an independent prognostic factor that greatly influences clinical management and survival outcomes. MIBC is a lethal malignancy, results in over 85% mortality within 2 years if left untreated or treated inadequately [4, 5]. Given these grave implications, the ability to predict muscle invasion could substantially enhance preoperative planning and patient outcomes.

Biopsy, being the gold standard for diagnosing muscle invasion, is an invasive method that struggles to definitively determine the extent of muscle layer infiltration due to challenges in obtaining a sufficient sample [3, 6]. This pitfall may pose serious problems, including the delay of radical treatment, disease progression and worsening oncological results [7]. Radiomics, as an emerging field, holds potential in converting digital imaging data into innumerable and mineable quantitative features that reveal pathophysiology [8]. Previous researches have shown that radiomics models utilizing conventional CT images can accurately forecast muscle invasion in BCa [9–12]. Dual-energy computed tomography (DECT) enables qualitative analysis of lesions and generation of material decomposition and virtual monochromatic images (VMIs) for providing additional value of disease diagnosis [13–15]. Material decomposition allows for the estimation of the concentration of specific elements within a region of interest, thereby distinguishing absorption characteristics of different elements [16–18]. Processed images such as VMIs have shown promising results in oncological imaging for tumor detection, characterization, and assessing therapy response [15]. Although radiomics, DECT material decomposition, and VMIs have demonstrated potential for characterizing various tumor types, their combined value in predicting muscle invasion in BCa remains unexplored. Consequently, this study aimed to investigate the optimal DECT-derived radiomics model for evaluating the muscle status of BCa and to explore the clinical significance of combining quantitative parameters and radiomics to preoperatively predict the muscle invasion.

Methods

Patients

This retrospective study was approved by the Institutional Ethics Committee, and the patient consent was waived. The study population was retrospectively enrolled patients who underwent dual-energy computed tomography urography (DECTU) for BCa staging purpose. Among these patients, those scanned between April 2021 and October 2023 were recruited. The inclusion criteria were confirmed by pathological examination as BCa and their CTU scans performed with dual-energy technique. The exclusion criteria were (I) incomplete imaging datasets, (II) incomplete clinicopathological diagnostic report, (III) inadequate image quality for analysis, (IV) lesions with a maximum diameter or thickness less than 10 mm, (V) radiation therapy or chemotherapy between CTU and pathological assessment. Ultimately, 126 patients were included. We randomly divided the cases into training ($n=88$) and test ($n=38$) cohorts with a ratio of 7:3. An overview workflow of this study is shown in Fig. 1.

DECT image acquisition

All CTU examinations were performed on a 256-row CT scanner (Revolution CT, GE HealthCare, Milwaukee, WI, USA). The acquisition parameters were as follows: Gemstone Spectral Imaging (GSI) mode with fast tube voltage switching (between 80 and 140 kVp); automatic exposure mode (GSI Assist) for selecting tube current to achieve noise index of 10; detector width of 80 mm; pitch of 0.992:1; tube rotation speed of 0.6 s/r. The contrast injection, with the amount of iodine intake proportional to patient's weight (500 mgI/kg) and at a maximum of 100 mL, was performed through a peripheral vein of the forearm at the injection speed of 3.0–4.0 ml/s, followed by appropriate amount of saline at the same rate to maintain a total injection time of 30 s. The non-ionic contrast agent (Ioversol, 350 mg/mL, Jiangsu Hengrui Pharmaceutical Co. Ltd., China) was used. The venous phase scan started at 70 s after administration of contrast medium. All venous phase images were reconstructed by using the adaptive statistical iterative reconstruction-V (ASIR-V) algorithm at 60% strength with slice thickness of 1.25 mm.

Quantitative parameter measurement

Spectral images were generated using the Advantage Workstation 4.7 dedicated to postprocessing (GE HealthCare) to reconstruct VMIs at 3 different energy levels (40,
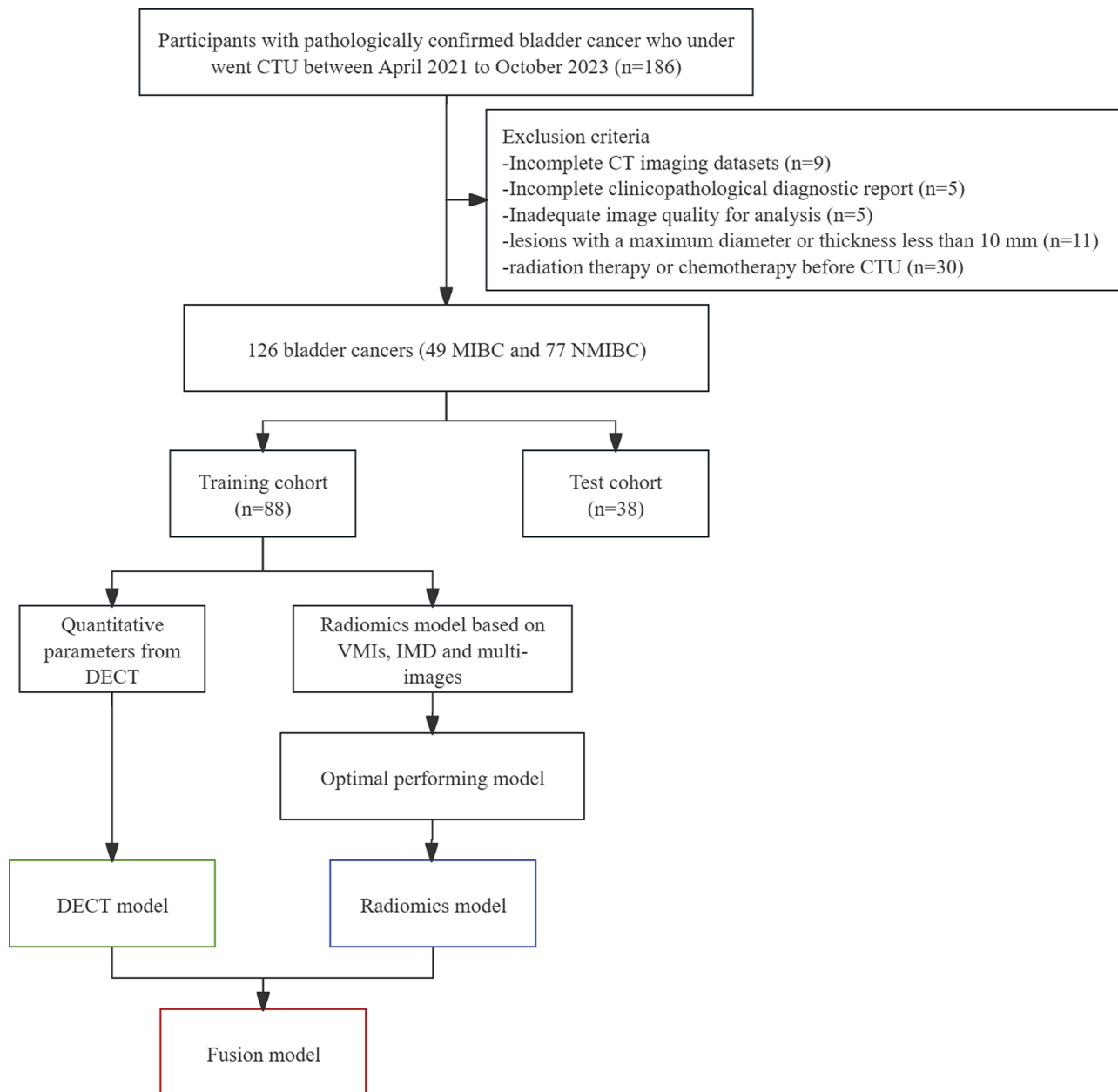
Fig. 1 Overview workflow of this study. DECT, Dual-energy CT; CTU, CT urography; MIBC, muscle-invasive bladder cancer; NMIBC, non-muscle-invasive bladder cancer; VMI, virtual monochromatic images; IMD, iodine material

70, and 100 keV), iodine (water)-based material decomposition (IMD), fat (water)-based and effective atomic number (Z_{eff}) images. Quantitative parameters were measured on three adjacent slices containing the largest area and the substantial part of the primary lesion, avoiding cystic area, calcification and necrosis. Two radiologists (with 2 and 10 years of experience in abdominal radiology, respectively) performed the quantitative measurements, unaware of the pathologic findings. The average values from the two radiologists were used for the final evaluation. The quantitative parameters from DECT

images included the following: (I) iodine concentration (IC) of the lesion (IC_{lesion}) and IC of descending aorta (IC_{aorta}) in the same layer, to calculate the normalized iodine concentration (NIC) = IC_{lesion}/ IC_{aorta}; (II) fat-water concentration (FC); (II) Z_{eff}.

Images segmentation

The 40, 70, 100 keV and IMD images were imported into the uAI Research Portal V1.1 software developed by Shanghai United Imaging Intelligence Co., Ltd. The tumor segmentation was delineated manually in three

dimensions slice-by-slice on the 40 keV axial images until the whole lesion was captured by a radiologist (with 2 years of experience in the abdominal imaging diagnosis), who was unaware of the clinical data and pathological results. To ensure accuracy, another senior radiologist (with 20 years of experience in abdominal imaging) verified and corrected all segmentation masks. Disagreements were resolved with consensus-based discussion. Subsequently, the resulting volume of interest (VOI) was copied to other types of images.

Radiomics model selection
Feature extraction
To address the interference caused by the non-uniform spatial resolution of CT images, we normalized all images using Z-score and resampled the voxel size spaced to $1 \times 1 \times 1$ mm through the B-spline interpolation, and gray values discretized into 25 bin-width. Features were extracted separately from each images using uAI Research Portal V1.1 software. These radiomic features were subdivided into the following classes: (1) first-order features; (2) shape features; (3) texture features, including gray level co-occurrence matrix (GLCM) features, gray level size zone matrix (GLSZM) features, gray level run length matrix (GLRLM) features, gray level difference matrix (GLDM) features, and neighboring gray tone difference matrix (NGTDM) features.

Feature selection and radiomics model construction
All radiomics features in the training cohort were standardized using the Z-score normalization method. To select the optimal radiomics features to construct the final model, a step-wise feature selection strategy was adopted. Firstly, we conducted the recursive feature elimination (RFE) via five-fold cross-validation to solve overfitting and classification accuracy problems. Then the least absolute shrinkage and selection operator (LASSO) was used to select the optimal radiomics features. Support Vector Machine (SVM) was utilized to construct radiomics models individually for single images (at 40, 70, 100 keV and IMD images) and multi-images (combining 40, 70, 100 keV and IMD images), aiming to identify the optimal performance radiomics model both in the training and test cohorts. A radiomics workflow is shown in Fig. 2.

Models building
DECT quantitative parameters selected through univariable and multivariate logistic regression analyses were utilized in building the DECT model. Then the most effective radiomics model was identified as the final choice. Finally, a fusion model integrating the radiomics scores (rad-score) from the radiomics model with the independent predictors from DECT model was developed using logistic regression algorithm. The fusion model was visually represented as a nomogram for individualized estimating the probability of MIBC in the training cohort.

Statistical analysis
Statistical analysis was performed using MedCalc version 20.2 (MedCalc, Ltd, Ostend, Belgium), R software (version 4.2.1), and SPSS version 26.0 (SPSS Inc., Chicago, IL, USA). Quantitative measurements from the monochromatic images and MD images in DECT were initially checked with the Shapiro-Wilk test for normal distribution. The normally distributed parameters were presented as mean±standard deviation (SD), while skewed variables were expressed as the median and inter quartile range (IQR). Variables were compared using independent sample t-test, Mann-Whitney U Test, chi-square tests, or Fisher exact test as appropriate. Variables with a p value<0.05 in the univariate analysis were identified as candidate variables for the multivariable binary logistic regression analysis. Subsequently, candidate variables were included as independent variables in a forward stepwise binary logistic regression to determine the independent predictors. A p value less than 0.05 was considered statistically significant.
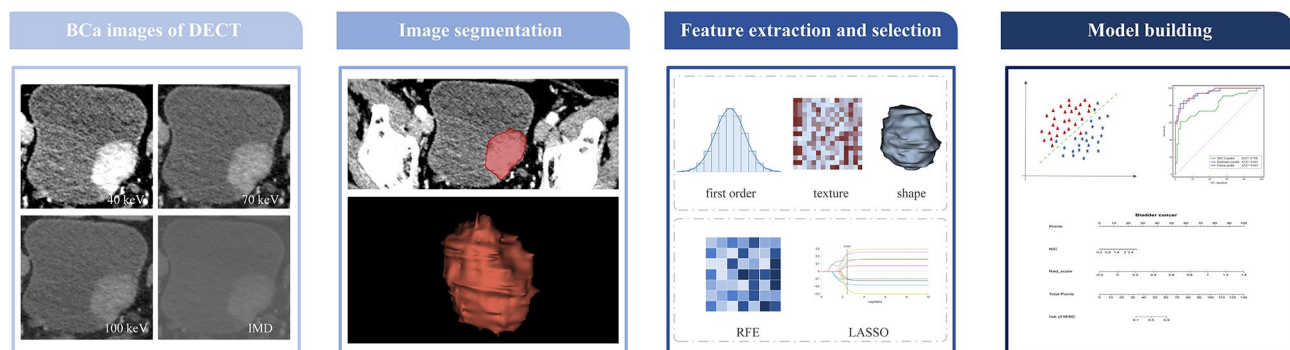

Fig. 2 A flow chart illustrating the process for building radiomics models in this study. RFE, recursion feature elimination; LASSO, least absolute shrinkage and selection operator

Table 1 Clinical data of bladder cancer patients in training and test cohorts

variables	Training cohort (*n* = 88)			Test cohort (*n* = 38)			*P* value[†]
	MIBC (*n* = 34)	NMIBC (*n* = 54)	*P* value[*]	MIBC (*n* = 15)	NMIBC (*n* = 23)	*P* value[*]	
Age (years)	69.00 (66.75, 76.50)	68.00 (63.00, 72.00)	0.077	69.00 (64.00, 75.00)	65.00 (59.00, 69.00)	0.083	0.103
Gender			0.341			0.371	0.987
Male	27	47		14	18		
Female	7	7		1	5		
Leision location			0.266			0.295	0.99
Side wall	20	38		8	17		
Trigone	14	16		7	6		
Diameter of lesion			0.698			0.436	0.104
≥ 3 cm	14	20		5	4		
< 3 cm	20	34		10	19		

MIBC, muscle-invasive bladder cancer; NMIBC, non-muscle-invasive bladder cancer; *Comparison between MIBC and low NMIBC. †Comparison between training and test cohorts

Table 2 Comparison of DECT quantitative parameters between MBIC and NMBIC

Variables	Training cohort (*n* = 88)			Test cohort (*n* = 38)		
	MIBC (*n* = 34)	NMIBC (*n* = 54)	*P* value	MIBC (*n* = 15)	NMIBC (*n* = 23)	*P* value
IC (mg/mL)	25.76 (20.97, 30.57)	28.45 (25.19, 35.37)	0.007	21.97 (19.62, 26.09)	29.49 (20.13, 35.36)	0.137
NIC	1.24 (0.72, 1.62)	0.68 (0.54, 0.87)	< 0.001	1.16 (0.57, 1.63)	0.66 (0.56, 0.91)	0.033
FC (mg/mL)	-1558.93 (-1816.74, -1220.38)	-1558.93 (-1816.74, -1220.38)	0.125	-1488.43 (-1837.06, -1364.02)	-1480.77 (-1714.00, -1189.89)	0.953
Z_{eff}	8.90 (8.65, 9.11)	8.82 (8.57, 8.99)	0.12	8.76 (8.68, 8.93)	8.75 (8.56, 8.93)	0.836

MIBC, muscle-invasive bladder cancer; NMIBC, non-muscle-invasive bladder cancer; IC, iodine concentration; NIC, normalized iodine concentration; FC, fat water concentration; Z_{eff}, effective atomic number

The receiver operating characteristic (ROC) curves were drawn, and sensitivity, specificity, accuracy, precision, and the area under the curve (AUC) were calculated respectively based on the R language to evaluate the diagnostic efficacy of the different models, and statistical differences between AUCs were compared using the DeLong test. Decision curves were utilized to compare the clinical usefulness of models.

Results
Patient characteristics
The clinical characteristics and DECT quantitative parameters of the 126 BCa patients are summarized in Tables 1 and 2, respectively. No significant differences were observed in age, gender, lesion location and diameter between the training and test cohorts (all *p* > 0.05). Moreover, regarding quantitative parameters, NIC showed significant difference between the MIBC and NMIBC in both cohorts with all *p* < 0.05, while IC was significantly different in the training cohort only with *p* < 0.05.

Feature selection and optimal radiomics based model screening
A total of 104 radiomics features were extracted from each VOI based on the 40, 70, 100 keV and IMD images. Following feature selection using RFE and Lasso methods, the optimal radiomics features of each image set remained. The diagnostic performances of the 5 radiomics models in the training and test cohorts are shown in Table 3. Notably, the diagnostic performance based on multi-image was the best differentiating MIBC and NMIBC in the training (AUC = 0.943) and test cohorts (AUC = 0.867), respectively.

Model building
DECT model
Among the four quantitative parameters (IC, NIC, FC and Z_{eff}) analyzed, the univariable analysis revealed that IC and NIC were significant risk factors for predicting muscle invasion. Further multivariable logistic regression analysis showed that NIC (OR, 25.426; 95% CI: 5.458-118.434; *P* < 0.001) was the sole independent predictor (Table 4). Consequently, NIC was used for the DECT model.

Table 3 The diagnostic performance of radiomics models

Cohort	Model	AUC (95% CI)	SEN	SPE	ACC	PRE
Training	40	0.937 (0.884, 0.990)	0.706	0.963	0.864	0.923
	70	0.893 (0.823, 0.964)	0.735	0.907	0.841	0.833
	100	0.868 (0.785, 0.951)	0.676	0.926	0.830	0.852
	IMD	0.932 (0.882, 0.982)	0.857	0.826	0.841	0.818
	Multi-image	0.943 (0.897, 0.990)	0.765	0.963	0.886	0.929
Test	40	0.838 (0.682, 0.993)	0.667	1.000	0.868	1.000
	70	0.846 (0.698, 0.995)	0.667	0.870	0.789	0.769
	100	0.800 (0.641, 0.959)	0.600	0.870	0.763	0.750
	IMD	0.777 (0.609, 0.944)	0.643	0.750	0.711	0.600
	Multi-image	0.867 (0.727, 1.000)	0.733	0.870	0.816	0.786

AUC, area under the curve; CI, confidence interval; SEN, sensitivity; SPE, specificity; ACC, accuracy; PRE, precision

Table 4 Independent factors for muscle invasion in bladder cancer

Variables	Univariate analysis			Multivariate analysis		
	OR	95% CI	*P* value	OR	95% CI	*P* value
IC (mg/mL)	0.920	0.861–0.983	0.014			
NIC	25.426	5.458-118.434	< 0.001	25.426	5.458-118.434	< 0.001
FC (mg/mL)	0.999	0.998-1.000	0.082			
Z_{eff}	3.312	0.817–13.436	0.094			

OR, odds ratio; CI, confidence interval; IC, iodine concentration; NIC, normalized iodine concentration; FC, fat water concentration; Z_{eff}, effective atomic number

Radiomics model
As previously mentioned, we selected the multi-image radiomics model based on the combination of the four sets of images (40, 70, 100 keV and IMD) as the optimal radiomics model.

Fusion model
We combined the independent predictor from the DECT model and the rad-score of the optimal radiomics model to construct the fusion model and develop a visual nomogram (Fig. 3).

Overall performance assessment
Model comparison
The performance of three models in distinguishing between MIBC and NMIBC is presented in Table 5, and the DeLong test comparing the performance of these models is shown in Table 6. ROC curves illustrated that the radiomics model was superior to the DECT model in predicting the muscle invasion status in the training cohort (AUC$_{radiomics}$= 0.943; AUC$_{DECT}$ =0.798) and the test cohort (AUC$_{radiomics}$ = 0.867, AUC$_{DECT}$ =0.704). Furthermore, the fusion model showed a slight additional improvement (AUC$_{training}$ = 0.943, AUC$_{test}$ = 0.893) as depicted in Fig. 4. Decision curves revealed that both the radiomics model and the fusion model provided a greater net benefit compared to the DECT model (Fig. 5).

Diameter-stratified analysis
In the test cohort, for lesions larger than 3 cm, both the fusion model and the radiomics model achieved AUC values of 0.800. Conversely, for lesions smaller than 3 cm, the fusion model exhibited improved predictive ability with an AUC value of 0.911, although the difference compared to the AUC value of the radiomics model (0.884) was not statistically significant. Notably, the DECT model had the lowest AUC values in both groups. Specific advantages of the diagnostic performance are outlined in Table 7.

Discussion
In this study, a fusion model integrating radiomics features and quantitative parameters derived from DECT was successfully developed to distinguish between MIBC and NMIBC. The results demonstrated that the fusion model exhibited the best predictive accuracy for muscle invasion, surpassing both the DECT and radiomics model. Additionally, this study highlighted the fusion model had potential advantages in identifying high-risk small lesions that may be challenging to identify. Our findings indicated that the fusion model held promise as a noninvasive tool for preoperative assessment of muscle status in BCa patients.

The iodine concentration (IC) derived from DECT enables the quantitative measurement of vascular enhancement in lesions, aiding in the differentiation of urothelial tumors from non-tumor lesions using IMD images [19, 20]. Our study demonstrated that the IC values of NMIBC were higher than those of MBIC, indicating discrimination potential. However, previous study had shown that IC values may be influenced by various factors, such as tumor size, blood volume, the degree of
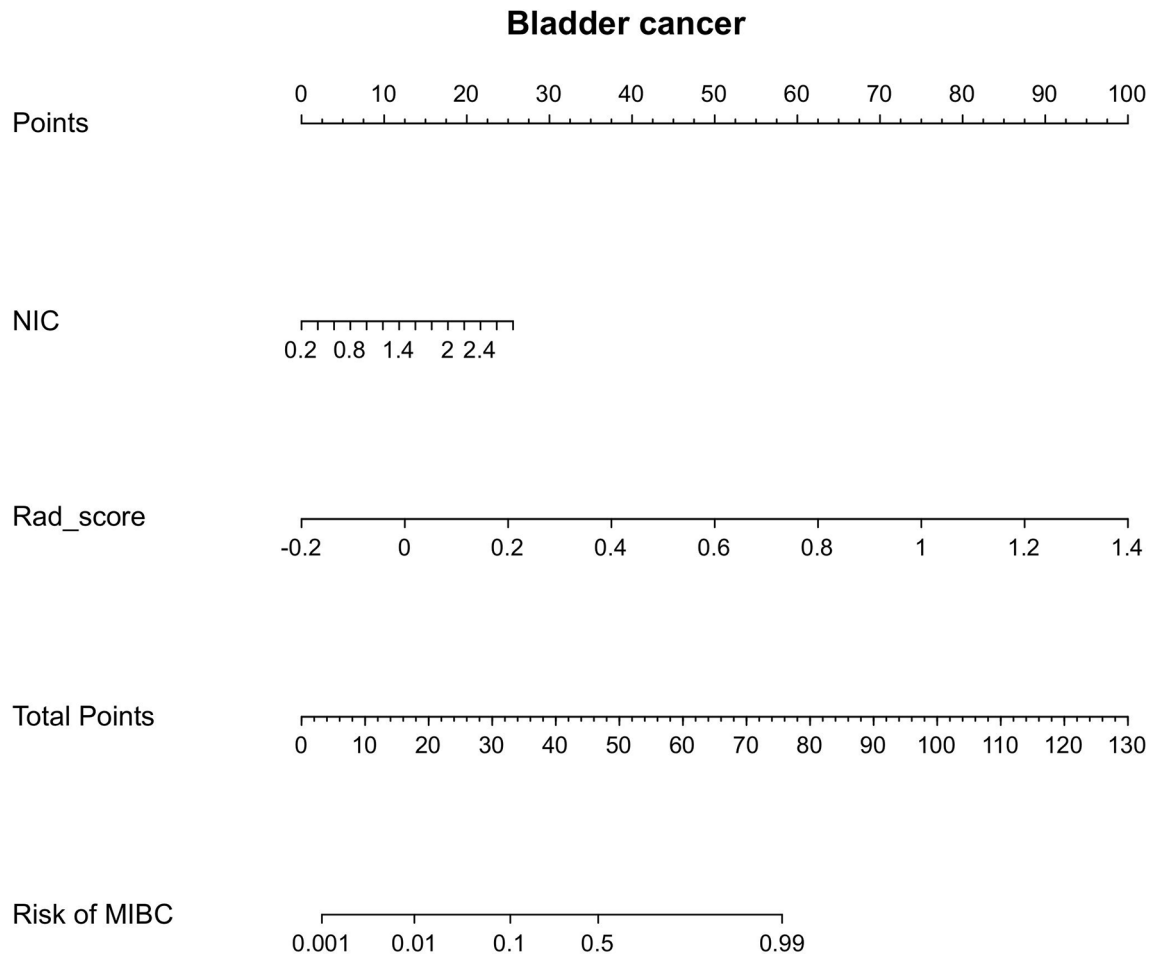
Bladder cancer

Fig. 3 The nomogram of the fusion model was constructed using the training cohort, incorporating NIC and rad-score of the multi-image radiomics model. NIC, normalized iodine concentration; Rad-score, radiomics scores; MIBC, muscle-invasive bladder cancer

Table 5 Comparison of AUCs between DECT, radiomics, and fusion models

	Model	AUC (95% CI)	SEN	SPE	ACC	PRE
Training cohort	DECT model	0.798 (0.699, 0.876)	0.618	0.944	0.818	0.875
	Radiomics model	0.943 (0.897, 0.990)	0.765	0.963	0.886	0.929
	Fusion model	0.943 (0.872, 0.981)	0.853	0.907	0.886	0.853
Test cohort	DECT model	0.704 (0.534, 0.841)	0.600	0.870	0.763	0.750
	Radiomics model	0.867 (0.727, 1.000)	0.733	0.870	0.816	0.786
	Fusion model	0.893 (0.749, 0.970)	0.800	0.913	0.868	0.857

AUC, area under the curve; CI, confidence interval; SEN, sensitivity; SPE, specificity; ACC, accuracy; PRE, precision

Table 6 DeLong test for the comparison of AUC values between different models

Cohort	Model comparison	Z statistic	P Value
Training	DECT vs. Radiomics	2.537	0.011
	Radiomics vs. Fusion	0.008	0.993
	DECT vs. Fusion	2.547	0.011
Test	DECT vs. Radiomics	1.336	0.182
	Radiomics vs. Fusion	0.286	0.775
	DECT vs. Fusion	1.656	0.098

enhancement, and differences in hemodynamics among individuals [21]. On the other hand, NIC could mitigate variations resulting from differences in circulation statuses among individuals, providing a more accurate representation of tumor tissue blood supply. In contrary to IC, the NIC values of MBIC were significantly higher than those of NMBIC. Our logistic regression analysis concluded that only NIC was an independent predictor of muscle status, effectively distinguishing MBIC from NMBIC with an AUC of 0.704.
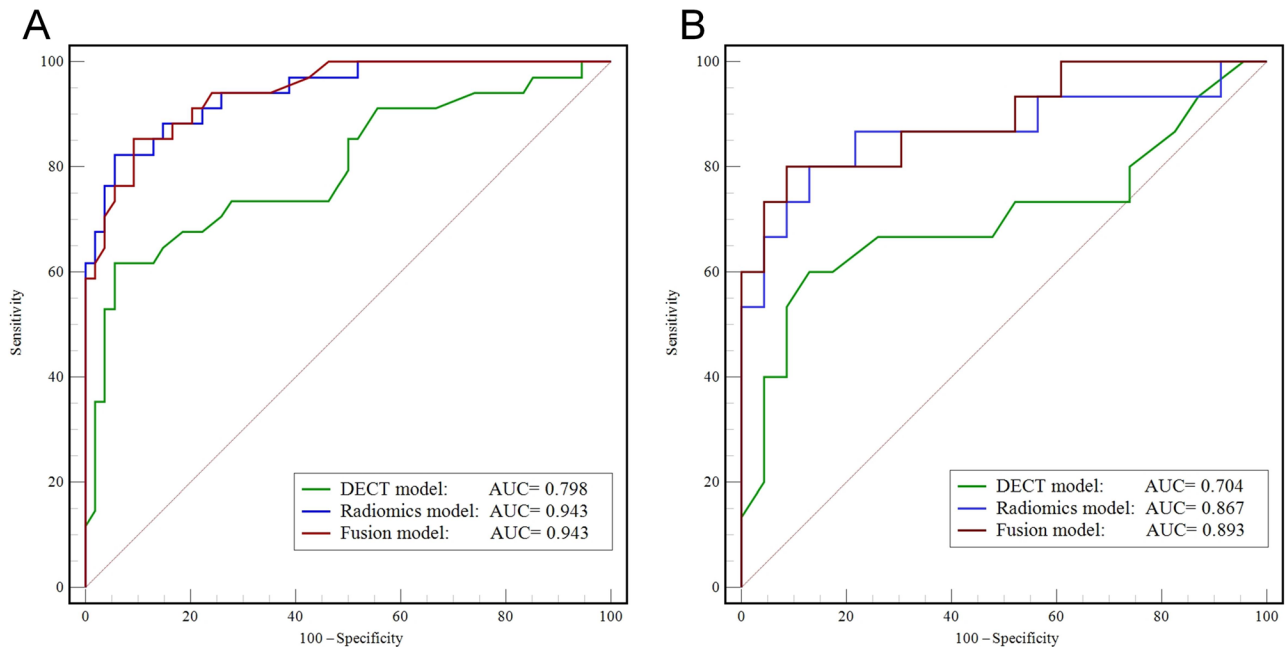
Fig. 4 Receiver operating characteristic curves for DECT, radiomic, and fusion models in training (**A**) and test cohorts (**B**).
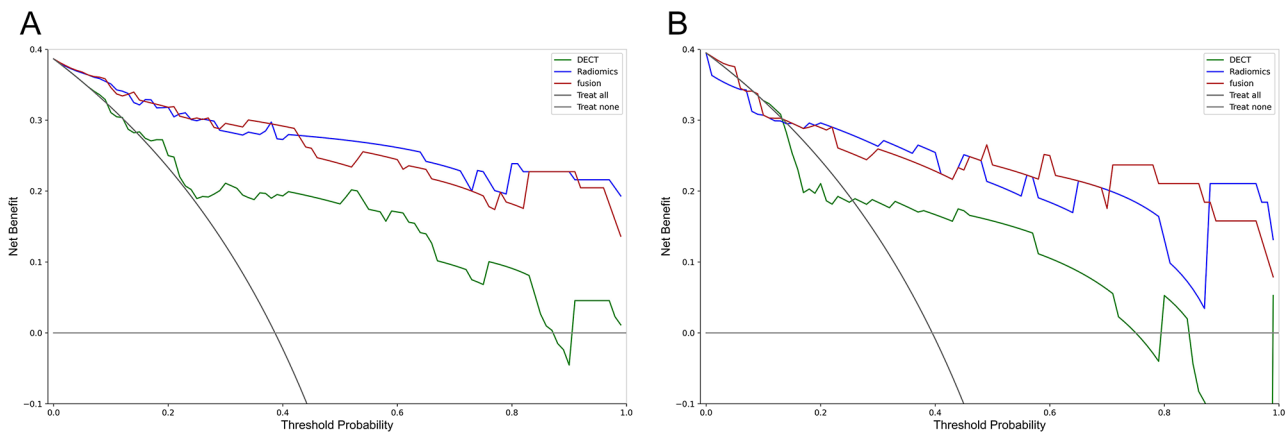

Fig. 5 Decision curves for DECT, radiomics, and fusion models in training (**A**) and test cohorts (**B**). Fusion model and radiomics model had higher net benefits than DECT model

Table 7 The diagnostic performance of three models in diameter-stratified analysis

Diameter	Model	AUC (95% CI)	SEN	SPE	ACC	PRE
≥ 3 cm	DECT model	0.625 (0.265, 0.903)	0.600	1.000	0.778	1.000
	Radiomics model	0.800 (0.422, 0.979)	0.800	1.000	0.889	1.000
	Fusion model	0.800 (0.422, 0.979)	0.800	1.000	0.889	1.000
< 3 cm	DECT model	0.726 (0.530, 0.874)	0.600	0.895	0.793	0.750
	Radiomics model	0.884 (0.711, 0.972)	0.900	0.895	0.897	0.818
	Fusion model	0.911 (0.745, 0.984)	0.800	0.895	0.862	0.800

AUC, area under the curve; CI, confidence interval; SEN, sensitivity; SPE, specificity; ACC, accuracy; PRE, precision

The existing CT-based radiomics models were based on conventional CT images to differentiate whether the tumor has invaded the muscular layer [9–11]. These studies demonstrated that radiomics models were effective in evaluating the invasiveness of muscle in BCa and outperformed visual assessments by radiologists. This underscores the potential of CT-based radiomics for evaluating muscle invasion in BCa. However, the impact of DECT on predicting muscle status remains unclear. Previous studies have highlighted the advantages of

multi-energy models derived from DECT. Al Ajmi et al. [22] introduced a multi-energy texture analysis utilizing VMIs ranging from 40 to 140 keV, capturing energy-dependent tissue attenuation changes. Using the same population, they improved the diagnostic accuracy of benign parotid tumors in comparison to the single-energy level of 65 keV (75–92%). Additionally, Forghani et al. [23] demonstrated that multi-energy texture analysis outperformed single-energy methods in evaluating lymph node metastasis in head and neck squamous cell carcinoma. Li et al. [24] utilized VMIs at 40, 65, and 100 keV obtained from both the arterial and venous phases to predict lymph node metastasis in gastric cancer. Their results showed that a nomogram based on multi-energy data exhibited superior predictive performance and added value compared to single-energy and clinical models. Considering CT physics and algorithms, low-energy images (40–70 keV) better reflect tissue enhancement features, whereas high-energy images (100–140 keV) represent non-enhanced tissue characteristics [25]. In our study, we selected the 40 keV to represent low-energy images, 100 keV for high-energy images, and 70 keV as an equivalent to a standard 120-kVp CT acquisition [26, 27]. IMD images selectively depict tissue perfusion and permeability, crucially linked to tumor angiogenesis and aggressiveness [28]. They not only facilitate the quantitative analysis of IC but also find successful application in radiomics, offering valuable insights for tissue characterization, diagnosing metastases, and predicting survival outcomes [29–33]. Furthermore, there is a notable deficiency in radiomics utilizing IMD images for muscle invasion characterization in BCa, which may enhance the predictive model performance by incorporating information on blood supply variations. Building on this premise, we incorporated IMD images into a multi-image analysis. The multi-image radiomics model incorporated features from images at 40,70,100 keV as well as IMD images, creating a holistic image dataset of the lesion that overcomed the constrains of single-energy imaging techniques. The results of our study indicated that the multi-image radiomics model outperformed radiomics models based solely on single images in distinguishing between MIBC and NMIBC. This suggested that multi-image radiomics model effectively captured variations in energy-dependent attenuation among different tissues and variations in blood perfusion, providing more comprehensive information than single image set alone.

In our study, the multi-image radiomics model exhibited superior predictive efficacy compared to the DECT model in forecasting the invasiveness of muscle. While quantitative parameters can capture microscopic details like blood flow and material composition, radiomics delves into both intra-tumor and inter-tumor heterogeneity by analyzing the entire lesion and its microenvironment without invasive conditions [34, 35]. The combination of these two aspects enhances the accuracy in revealing the fundamental characteristics of the lesion. Thus, we conducted a novel fusion model that combines the rad-score of radiomics model with NIC for the first time to preoperatively forecast muscle invasiveness of BCa. The fusion model showcased improved accuracy from 82 to 87%, with the sensitivity and specificity increasing from 73% and 87–80% and 91%, respectively. Tumor size holds prognostic and predictive significance in NMIBC and is considered as a critical feature in determining muscle invasion. Then, we separately evaluated lesions stratified by diameter [36, 37]. Our findings showed that the fusion model had the largest AUC compared to both DECT and radiomics models in lesions smaller than 3 cm. These results proposed that the fusion model may offer significant value in the assessment of small lesions.

This study has several limitations. Firstly, it depended on manual tumor segmentation, a process susceptible to subjectivity introduced by radiologists. Secondly, the adoption of DECT was lower than that of conventional CT, leading to a decreasing number of patients receiving both pathological biopsies and DECT. Consequently, our imaging options were limited to single-mode techniques. Thirdly, the utilization of only venous-phase CT images may limit the diagnostic performance of the models, suggesting potential enhancement by incorporating multiphase CT images.

In conclusion, the multi-image radiomics model outperformed radiomics models based on the individual 40, 70, 100 keV and IMD images in distinguishing between MBIC and NMBIC. The fusion model, which combines the radiomics model and NIC, demonstrated improved predictive performance for muscle invasion compared to both the DECT and radiomics models, although the difference was not statistically significant. This innovative method holds promise in unraveling the heterogeneity of muscle status in BCa and in providing personalized medical care for MBIC patients efficiently and scientifically.

Abbreviations

BCa	Bladder cancer
NMIBC	Non-muscle-invasive bladder cancer
MIBC	Muscle-invasive bladder cancer
DECT	Dual-energy CT
IMD	Iodine-based material-decomposition
ROC	Receiver operating characteristic
DCA	Decision curve analysis
NIC	Normalized iodine concentration
AUC	Area under the curve
Zeff	Effective atomic number
SVM	Support vector machine

Declarations

Ethics approval and consent to participate
The study was approved by the Ethics Committee of the First Affiliated Hospital of Dalian Medical University (no. PJ-KS-KY-2019-110). Written informed consent was obtained from all subjects (patients) in this study.

Consent for publication
Not applicable.

Competing interests
The authors declare no competing interests.

Author details
[1]Department of Radiology, First Affiliated Hospital of Dalian Medical University, No.193, Lianhe Road, Xigang District, Dalian, China
[2]CT Research, GE Healthcare, Dalian, China
[3]Department of Urology, First Affiliated Hospital of Dalian Medical University, Dalian, China

References
1. Crocetto F, Buonerba C, Caputo V, Ferro M, Persico F, Trama A, Iliano E, Rapisarda S, Bada M, Facchini G, et al. Urologic malignancies: advances in the analysis and interpretation of clinical findings. Future Sci OA. 2021;7(4):Fso674.
2. Sung H, Ferlay J, Siegel RL, Laversanne M, Soerjomataram I, Jemal A, Bray F. Global Cancer statistics 2020: GLOBOCAN estimates of incidence and Mortality Worldwide for 36 cancers in 185 countries. Cancer J Clin. 2021;71(3):209–49.
3. Rouprêt M, Seisen T, Birtle AJ, Capoun O, Compérat EM, Dominguez-Escrig JL, Gürses Andersson I, Liedberg F, Mariappan P, Hugh Mostafid A, et al. European Association of Urology Guidelines on Upper urinary tract Urothelial Carcinoma: 2023 update. Eur Urol. 2023;84(1):49–64.
4. Stein JP, Skinner DG. Radical cystectomy for invasive bladder cancer: long-term results of a standard procedure. World J Urol. 2006;24(3):296–304.
5. Ferro M, Chiujdea S, Musi G, Lucarelli G, Del Giudice F, Hurle R, Damiano R, Cantiello F, Mari A, Minervini A, et al. Impact of age on outcomes of patients with pure Carcinoma in situ of the Bladder: multi-institutional cohort analysis. Clin Genitourin Cancer. 2022;20(2):e166–72.
6. Powles T, Bellmunt J, Comperat E, De Santis M, Huddart R, Loriot Y, Necchi A, Valderrama BP, Ravaud A, Shariat SF, et al. Bladder cancer: ESMO Clinical Practice Guideline for diagnosis, treatment and follow-up. Ann Oncol. 2022;33(3):244–58.
7. Hansel DE, Amin MB, Comperat E, Cote RJ, Knüchel R, Montironi R, Reuter VE, Soloway MS, Umar SA, Van der Kwast TH. A contemporary update on pathology standards for bladder cancer: transurethral resection and radical cystectomy specimens. Eur Urol. 2013;63(2):321–32.
8. Bera K, Braman N, Gupta A, Velcheti V, Madabhushi A. Predicting cancer outcomes with radiomics and artificial intelligence in radiology. Nat Rev Clin Oncol. 2022;19(2):132–46.
9. Cui Y, Sun Z, Liu X, Zhang X, Wang X. CT-based radiomics for the preoperative prediction of the muscle-invasive status of bladder cancer and comparison to radiologists' assessment. Clin Radiol. 2022;77(6):e473–82.
10. Zhang G, Xu L, Zhao L, Mao L, Li X, Jin Z, Sun H. CT-based radiomics to predict the pathological grade of bladder cancer. Eur Radiol. 2020;30(12):6749–56.
11. Garapati SS, Hadjiiski L, Cha KH, Chan HP, Caoili EM, Cohan RH, Weizer A, Alva A, Paramagul C, Wei J, et al. Urinary bladder cancer staging in CT urography using machine learning. Med Phys. 2017;44(11):5814–23.
12. Ferro M, Falagario UG, Barone B, Maggi M, Crocetto F, Busetto GM, Giudice FD, Terracciano D, Lucarelli G, Lasorsa F et al. Artificial Intelligence in the Advanced Diagnosis of Bladder Cancer-Comprehensive Literature Review and Future Advancement. *Diagnostics (Basel)* 2023, 13(13).
13. Lin XZ, Wu ZY, Tao R, Guo Y, Li JY, Zhang J, Chen KM. Dual energy spectral CT imaging of insulinoma-value in preoperative diagnosis compared with conventional multi-detector CT. Eur J Radiol. 2012;81(10):2487–94.
14. Parakh A, Patino M, Muenzel D, Kambadakone A, Sahani DV. Role of rapid kV-switching dual-energy CT in assessment of post-surgical local recurrence of pancreatic adenocarcinoma. Abdom Radiol (NY). 2018;43(2):497–504.
15. Simons D, Kachelriess M, Schlemmer HP. Recent developments of dual-energy CT in oncology. Eur Radiol. 2014;24(4):930–9.
16. Li Q, Song Z, Zhang D, Li X, Liu Q, Yu J, Wen Y, Zhang J, Ren X, Li Z, et al. Diagnostic accuracy of dual-energy computed tomography-based nomogram for differentiating papillary thyroid microcarcinomas from micronodular goiters. Quant Imaging Med Surg. 2023;13(6):3428–40.
17. Li Z, Chen Y, Zhang Y, Shi J, Wan Y. Quantitative energy spectrum CT in differential diagnosis of aldosterone-producing adenoma and cortisol-producing adenoma. Quant Imaging Med Surg. 2023;13(8):5012–21.
18. Qiu L, Hu J, Weng Z, Liu S, Jiang G, Cai X. A prospective study of dual-energy computed tomography for differentiating metastatic and non-metastatic lymph nodes of colorectal cancer. Quant Imaging Med Surg. 2021;11(8):3448–59.
19. Kato T, Uehara K, Ishigaki S, Nihashi T, Arimoto A, Nakamura H, Kamiya T, Oshiro T, Ebata T, Nagino M. Clinical significance of dual-energy CT-derived iodine quantification in the diagnosis of metastatic LN in colorectal cancer. Eur J Surg Oncol. 2015;41(11):1464–70.
20. Hansen C, Becker CD, Montet X, Botsikas D. Diagnosis of urothelial tumors with a dedicated dual-source dual-energy MDCT protocol: preliminary results. AJR Am J Roentgenol. 2014;202(4):W357–364.
21. Zhu Y, Feng B, Cai W, Wang B, Meng X, Wang S, Ma X, Zhao X. Prediction of Microvascular Invasion in Solitary AFP-Negative Hepatocellular Carcinoma ≤ 5 cm using a combination of imaging features and quantitative dual-layer spectral-detector CT parameters. Acad Radiol. 2023;30(Suppl 1):S104–16.
22. Al Ajmi E, Forghani B, Reinhold C, Bayat M, Forghani R. Spectral multi-energy CT texture analysis with machine learning for tissue classification: an investigation using classification of benign parotid tumours as a testing paradigm. Eur Radiol. 2018;28(6):2604–11.
23. Forghani R, Chatterjee A, Reinhold C, Pérez-Lara A, Romero-Sanchez G, Ueno Y, Bayat M, Alexander JWM, Kadi L, Chankowsky J, et al. Head and neck squamous cell carcinoma: prediction of cervical lymph node metastasis by dual-energy CT texture analysis with machine learning. Eur Radiol. 2019;29(11):6172–81.
24. Li J, Dong D, Fang M, Wang R, Tian J, Li H, Gao J. Dual-energy CT–based deep learning radiomics can improve lymph node metastasis risk prediction for gastric cancer. Eur Radiol. 2020;30(4):2324–33.
25. Bicci E, Mastrorosato M, Danti G, Lattavo L, Bertelli E, Cozzi D, Pradella S, Agostini S, Miele V. Dual-energy CT applications in urinary tract cancers: an update. Tumori. 2023;109(2):148–56.
26. Matsumoto K, Jinzaki M, Tanami Y, Ueno A, Yamada M, Kuribayashi S. Virtual monochromatic spectral imaging with fast kilovoltage switching: improved image quality as compared with that obtained with conventional 120-kVp CT. Radiology. 2011;259(1):257–62.
27. Forghani R. An update on advanced dual-energy CT for head and neck cancer imaging. Expert Rev Anticancer Ther. 2019;19(7):633–44.
28. Kim YN, Lee HY, Lee KS, Seo JB, Chung MJ, Ahn MJ, Park K, Kim TS, Yi CA. Dual-energy CT in patients treated with anti-angiogenic agents for non-small cell lung cancer: new method of monitoring tumor response? Korean J Radiol. 2012;13(6):702–10.
29. Zhu Y, Wang P, Wang B, Jiang Z, Li Y, Jiang J, Zhong Y, Xue L, Jiang L. Dual-layer spectral-detector CT for predicting microsatellite instability status and prognosis in locally advanced gastric cancer. Insights Imaging. 2023;14(1):151.

30. Zegadło A, Żabicka M, Kania-Pudło M, Maliborski A, Różyk A, Sośnicki W. Assessment of Solitary Pulmonary nodules based on virtual monochrome images and iodine-dependent images using a single-source dual-energy CT with fast kVp switching. J Clin Med 2020, 9(8).

31. Lenga L, Bernatz S, Martin SS, Booz C, Solbach C, Mulert-Ernst R, Vogl TJ, Leithner D. Iodine map Radiomics in breast Cancer: prediction of metastatic status. Cancers (Basel) 2021, 13(10).

32. Zhou Y, Su GY, Hu H, Ge YQ, Si Y, Shen MP, Xu XQ, Wu FY. Radiomics analysis of dual-energy CT-derived iodine maps for diagnosing metastatic cervical lymph nodes in patients with papillary thyroid cancer. Eur Radiol. 2020;30(11):6251–62.

33. Choe J, Lee SM, Do KH, Lee JB, Lee SM, Lee JG, Seo JB. Prognostic value of radiomic analysis of iodine overlay maps from dual-energy computed tomography in patients with resectable lung cancer. Eur Radiol. 2019;29(2):915–23.

34. Jamal-Hanjani M, Quezada SA, Larkin J, Swanton C. Translational implications of tumor heterogeneity. Clin Cancer Res. 2015;21(6):1258–66.

35. Gerlinger M, Rowan AJ, Horswell S, Math M, Larkin J, Endesfelder D, Gronroos E, Martinez P, Matthews N, Stewart A, et al. Intratumor heterogeneity and branched evolution revealed by multiregion sequencing. N Engl J Med. 2012;366(10):883–92.

36. Zhang R, Jia S, Zhai L, Wu F, Zhang S, Li F. Predicting preoperative muscle invasion status for bladder cancer using computed tomography-based radiomics nomogram. BMC Med Imaging. 2024;24(1):98.

37. Huang X, Wang X, Lan X, Deng J, Lei Y, Lin F. The role of radiomics with machine learning in the prediction of muscle-invasive bladder cancer: a mini review. Front Oncol. 2022;12:990176.

Publisher's note